

Characterising the Internal Wave Field
of
Barkley Canyon
(Rough)

Kurtis Anstey
V00939802

Department of Physics and Astronomy
University of Victoria
July 22, 2021

Dr. Jody Klymak (University of Victoria)
Dr. Steven Mihal (Ocean Networks Canada)
Dr. Richard Thomson (Institute of Ocean Sciences)

Table of Contents

List of Figures	3
1 Abstract	4
2 Introduction	5
3 Theory	8
4 Data	10
5 Methods	14
5.1 Frequency spectra	14
5.2 Critical slope analysis	15
5.3 Near-inertial slab model	16
5.4 Dissipation estimates	17
6 Results	18
6.1 Mean currents	18
6.2 Tidal currents and internal waves	20
6.3 Frequency response	22
6.4 Slope effects	24
6.5 Canyon effects	27
6.6 Subdiurnal & tidal seasonality	28
6.7 Near-inertial seasonality	30
6.8 Continuum seasonality	31
7 Discussion	32
8 Conclusions	33
9 Appendix A: Inter-annual	34
10 References	39

List of Figures

1	Internal wave processes	6
2	Internal waves and topography	7
3	Radiating internal waves in a lab	9
4	Bathymetry of Barkley Canyon	11
5	Site topography	13
6	Averaged stratification and WKB-stretch scaling	14
7	Velocities - Low-pass - 2013	19
8	Velocities - High-pass - 2013	21
9	Power spectra - 2013	23
10	Rotary spectra - 2013	23
11	Depth-band PSD - Upper Slope - 2013	35
12	Depth-band rotary spectra - Upper Slope - 2013	36
13	Depth-band PSD - Axis - 2013	37
14	Depth-band rotary spectra - Axis - 2013	38

1 Abstract

This research characterises the internal wave field at Barkley Canyon, to provide information regarding regional mixing processes and what drives them. We make use of four overlapping years of ADCP time-series data, at both slope and canyon sites, to build on a body of research regarding interactions of internal waves with irregular topography, and associated processes, in the Vancouver Island Continental Shelf (VICS) region. This research is important for understanding transport of nutrients, heat, O_2 , and CO_2 , which affect climate drivers like the overturning circulation, as well as biological productivity. Key findings indicate that individual frequency constituents and bands experience unique seasonality and topographical effects. Additionally, a topographically influenced internal wave continuum state, as compared to canonical GM79 theory, could further influence slope and canyon mixing contributions.

2 Introduction

Internal waves are slow-moving, low-frequency, underwater gravity waves that exist due to density gradients in the ocean interior (Garrett & Munk, 1979). They can have wavelengths up to kilometres long, and oscillate in a range between the Coriolis (inertial, f) and Brunt–Väisälä (buoyancy, N) frequencies (Garrett & Munk, 1979). They are caused by wind, or tides and currents moving over irregular seafloor topography, generating waves that travel through the stratified ocean (Hendershott & Garrett, 2018). These waves propagate through the depths, where incident topography can cause them to scatter, reflect, or break (Martini et al., 2013).

As the wind and tides are ever-present drivers of ocean processes, internal waves are common features. As early as the mid-19th century, scientists such as Stokes and Rayleigh were discussing fluid density and stratification, essential for internal wave propagation (Garrett & Munk, 1979). Internal waves were reported as consistent noise in early 20th-century hydrocast readings, and Ekman made note of them in his seminal theories on fluid mechanics (Garrett & Munk, 1979). Later, Garrett and Munk (1979) developed the canonical Garrett-Munk (GM) spectrum to define the characteristic frequency and wavenumber continuum of open-ocean internal waves. As the capabilities of instruments improved, scientists continued to uncover the importance of internal waves to both small- and large-scale physical processes (Figure 1; Garrett & Munk, 1979). This led to a branching of internal wave research, with recent studies focusing on important concepts such as internal wave generation and dissipation (Terker et al., 2014; Kunze, 2017), forcing response due to seasonal weather variability (Alford et al., 2012; Thomson & Krassovski, 2015), and the scattering and reflection of internal waves at slopes and canyons (Nash et al., 2004; Kunze et al., 2012; Gemmrich & Klymak, 2015).

Notable effects near irregular topography have highlighted these sites as drivers of internal wave activity. As internal waves and tides approach seamounts, slopes, or canyons, their energy is focused, cascading from low- to high-frequency processes, and eventually dissipate as heat (Garrett & Munk, 1979). This dissipation leads to an energetic local environment, evident as turbulent processes on the micro- (less than 1 m vertical) and fine-scales (1 m to 100 m vertical) (Garrett & Munk, 1979; Kunze et al., 2012). This then contributes to regional transport of energy and momentum, and the mixing of heat, pollutants, and biological constituents (Kunze et al., 2012). Furthermore, internal waves help to set ocean stratification, layers that drive large-scale systems such as the overturning circulation (Garrett & Munk, 1979). As such, understanding internal wave interactions with topography is important for predicting changes

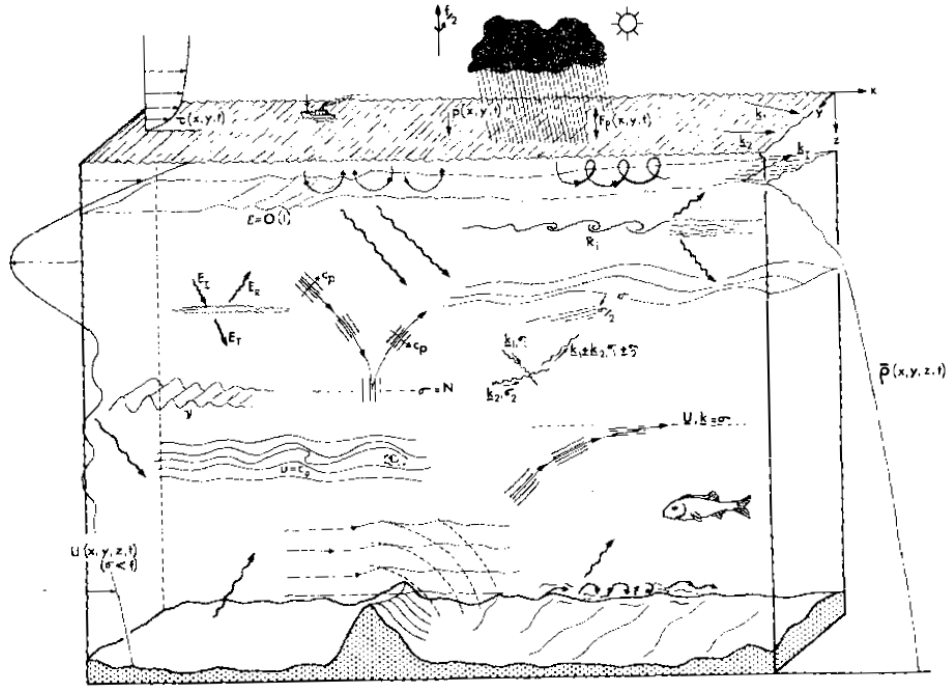


Figure 1: Generalised depiction of internal wave processes in the ocean, as envisioned by Garrett and Munk (1979).

in the coupled ocean-atmosphere climate system (Garrett & Munk, 1979).

Topography focused internal wave studies are numerous, and have been ongoing at locations such as the Hawaiian ridge (Alford et al., 2007), the slopes of the South China Sea (Klymak et al., 2011), and in slope-incising canyons of the northeastern Pacific (Allen et al., 2001; Carter & Gregg, 2002; Kunze et al., 2012; Terker et al., 2014). Canyons and their adjacent slopes have been identified as hot spots of internal wave activity, that not only generate (Carter & Gregg, 2002), but also dissipate internal waves and tides (Allen et al., 2001; Kunze et al., 2002). Research at Monterey Canyon, alone, has produced results regarding the scattering and reflection of internal waves and tides on critical slopes (Figure 2; Kunze et al., 2012), the presence of internal-bores and near-bottom turbulent layers that drive mixing (Carter & Gregg, 2002; Kunze et al., 2002), and correlation between topography and increased dissipation and generation of internal waves and tides (Terker et al., 2014). These results, among others, each highlight internal waves interactions with topography as drivers of regional physical processes.

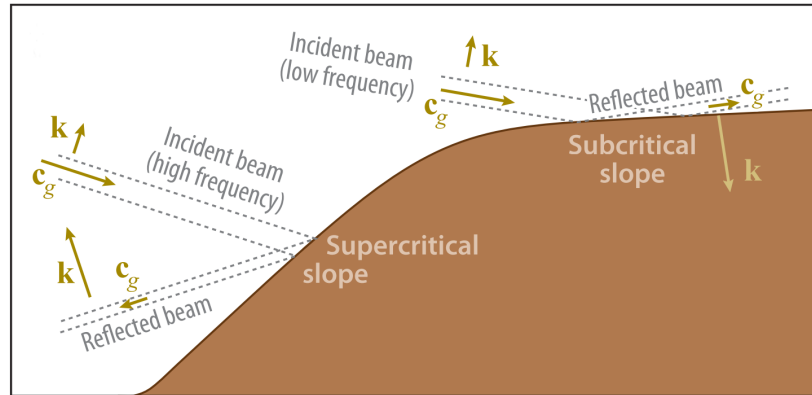


Figure 2: Graphic depiction of internal wave interactions with irregular topography. Adapted from Lamb (2014).

In Canada, research in the Pacific is often focused on the Vancouver Island Continental Shelf (VICS). Regional studies have led to results on seasonal wind forcing for near-inertial internal waves (Alford et al., 2012), potential evidence of non-linear wave-wave interaction between inertial internal waves and semidiurnal internal tides (Mihaly et al., 1998), locally generated coastal trapped waves (CTW) of diurnal frequency (Thomson & Crawford, 1982), and regional currents associated with the northeast Pacific current cycle (Thomson & Krassovski, 2015). The seasonally variable currents have been associated with observations of vorticity stretching and upwelling at the head of Barkley Canyon, suggesting considerable canyon influence on local water properties and transport of biological constituents (Allen et al., 2001); the VICS is one of the world's most productive shelf environments. As such, further research at Barkley Canyon is necessary to improve understanding of important regional mixing processes, and what drives them.

Despite considerable research into physical processes at the VICS, a better understanding of internal wave interactions at the bordering continental slope and its incising canyons is necessary for accurately predicting regional mixing contributions and resultant climate effects and biological productivity. As such, this research will evaluate horizontal velocity data from two sites, one in Barkley Canyon and another on the nearby slope, to provide information regarding regional mixing processes and their generation mechanics. This will include an analysis of seasonal variability in regional mean currents, tides, and winds, to identify forcing. Forcing will be correlated to observable internal wave events on the slope and within the canyon, and association expanded to

dissipative processes that may affect regional systems. Finally, the state of the internal wave continuum will be characterised through a comparison with accepted GM theory, to highlight topographic dependencies of the internal wave field.

3 Theory

Internal waves are dependent on stratification, but do not require a sharp density interface to exist; they are commonly found in continuously stratified fluids like the ocean interior, where density, $\rho(z)$, is a function of depth (z). The following is largely a concise adaptation of a much more detailed discussion by Kundu & Cohen (2008), cited here for clarity.

Stratification requires that internal wave theory consider buoyancy effects through depth. In order to describe the oscillatory motion of a fluid parcel displaced vertically, it is necessary to introduce the buoyancy frequency, N , as:

$$N^2 = -\frac{g}{\rho_0} \frac{\partial \rho(z)}{\partial z} \quad (1)$$

where g is the acceleration due to gravity, and ρ_0 is a reference density at a particular depth. Buoyancy effects allow for a consideration of wave propagation through a continuously stratified fluid, and suggests that internal waves are non-isotropic. Thus, for a 2D approximation, wavenumber (k and m), frequency (ω), and phase and group velocities (\mathbf{c}_p and \mathbf{c}_g) must be defined with vector qualities due to the importance of both magnitude and direction.

Furthermore, internal waves in a continuously stratified fluid are rotational processes. This further necessitates a derivation of a dispersion relation with appropriate buoyancy considerations and in vector form. However, as N varies with depth, this is a difficult task. If $N(z)$ is allowed to change with depth, vertical propagation of internal waves can be limited at 'turning depths'. The effect is better described by the Wentzel–Kramers–Brillouin (WKB) approximation, where for a single propagating wave ω and k are held fixed, while N is free to affect an adaptive vertical wavenumber, m (Garrett & Munk, 1979). For a simple model, however, it is found that the vertical change in N is slow enough, locally, that as a final leading assumption N can be considered depth independent.

Now, for a steady stratified flow with vertical velocity, w , where:

$$w = w_0 e^{i(kx + mz - \omega t)} \quad (2)$$

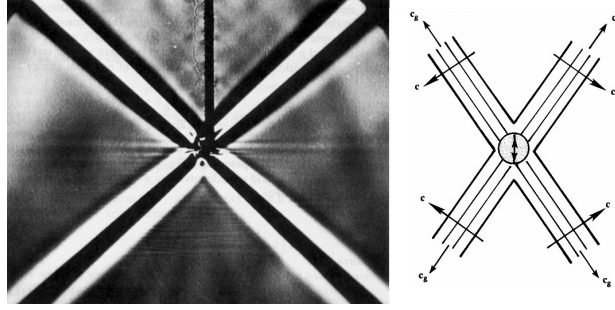


Figure 3: A photograph and graphic showing laboratory evidence for the symmetric radiation of 2D internal waves, from a source. Note the perpendicular phase and group velocities. Adapted from Kundu & Cohen (2008).

and w_0 is an amplitude, x the horizontal distance, and t is time, some algebraic work results in a surprisingly simple expression for the dispersion relation, where:

$$\omega = N \cos(\theta) \quad (3)$$

and θ is the angle from the x -axis to the direction of the phase velocity, \mathbf{c}_p . This suggests that not only does the frequency of internal waves only depend on the direction of the wavenumber (in θ), but that N is the limiting maximum frequency of internal waves. The maximum frequency of $\omega_{\max} = N$ is then found at the limit of $\theta = 0$, when the wavenumber is only horizontal, i.e. $m = 0$, so that the water column oscillates vertically. Furthermore, considering rotation effects, it is found that the limiting minimum frequency for internal waves, ω_{\min} , is the local Coriolis parameter, f (Garrett & Munk, 1979).

As a result of the directional dispersion relation, the group velocity, \mathbf{c}_g , is found to be perpendicular to the phase speed, \mathbf{c}_p ; i.e. their \mathbf{e}_1 components are the same, while their \mathbf{e}_3 components are opposite. This is interesting in that lines of phase propagate perpendicularly away from the beam of energy propagation associated with group velocity. It follows that in 2D, internal waves radiate group velocity outward from a source in four directions, each at an angle θ from vertical (Figure 3). This angle is defined by $\cos(\theta) = \omega/N$, with one beam in each quadrant, and phase radiating perpendicularly outward from each. From this result it follows that the energy flux per unit area is $\mathbf{F} = \mathbf{c}_g E$, where E is the energy per unit volume.

At this point, a discussion of internal waves mechanics can only continue by methodically eliminating governing assumptions. However, it is sufficient for the purposes of this paper to have provided a concise description of the fun-

damental theory. As a takeaway simplification, internal waves are sub-surface waves that propagate with perpendicular phase and group velocities outward from a source, exist due to density gradients in a fluid, and are contributors to significant physical processes such as large-scale mixing and transport.

4 Data

The obtained dataset is unique for both temporal and spatial consideration. Located at approximately 48.33°N 126.03°W, Barkley Canyon is about 75 km southwest of Vancouver Island, incising the continental slope and shelf with a rim and axis at depths of approximately -400 and -1000 m, respectively (Figure 4; Barkley Canyon, 2013). Spread across the topography of the canyon, Acoustic Doppler Current Profilers (ADCP) provide current data for Ocean Networks Canada (ONC), which maintains an array of instruments as part of the extensive NEPTUNE cabled observatory (ONC, 2013). ADCP emit acoustic beams that triangulate Doppler shifts in the water column, providing directional velocity data through time. For the selected instruments the available time series is over ten years, much longer than is typically available for internal wave research, allowing for analysis of both seasonal and multi-annual trends. Furthermore, the broad placement of ADCPs, both in the canyon and on the nearby slope, allows for a comparative spatial analysis of internal wave effects at varied topography; a typically difficult prospect with single instruments or dropped observations.

For Barkley Canyon, the ONC Oceans 2.0 data portal offers publicly available data spanning over 10 years, from 2009 to present. The ADCP and their data are maintained, configured, and cleaned for distribution by ONC. Relevant ADCP were chosen at the Axis (75 and 55 kHz) and Upper Slope (75 kHz) sites. The 75 kHz Teledyne RDI instruments have a sampling rate of 2 seconds; the 55 kHz Nortek instrument has a pulsed sampling rate of six 18-second interval pings followed by a 4.5-minute delay. The Upper Slope 75 kHz ADCP sits below the VICS shelf-break at a depth of -378 metres (Figure 5), 75 km SW from Vancouver Island and 15 km NW of Barkley Canyon. The Axis 75 & 55 kHz ADCPs are located on the bottom of Barkley Canyon at a depth of -968 metres (Figure 5), about mid-length along the canyon at a sharp bend where a narrow north-south channel runs between adjacent outcrops to the east and west. Vertical resolution is 8 m depth bins for the 75 kHz instruments, and 20 m depth bins for the 55 kHz instrument.

To assess data quality and coverage, an initial quality check (error velocity, correlation, and backscatter intensity for both depth and time, based on ONC

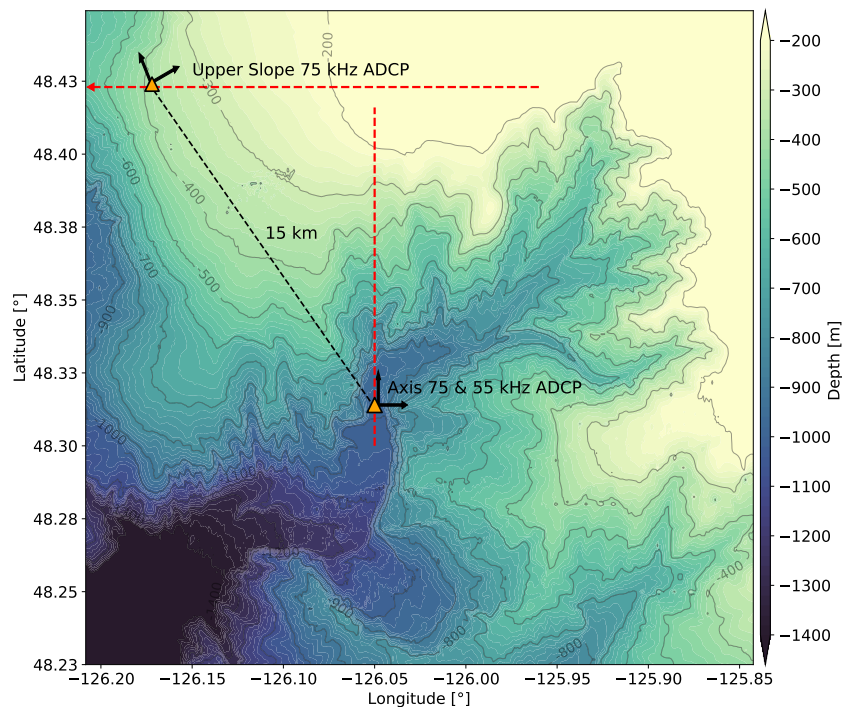


Figure 4: Bathymetry of Barkley Canyon. 3-arc-second mean sea level depth data obtained from the NOAA National Centre for Environmental Information. Perpendicular arrows at each site show rotated Cartesian coordinate systems, and the dashed red lines show the bathymetry cross-sections used for Figure 5 (cite).

deployment parameters) was performed with both raw and averaged 1-hour data. Afterwards, complete datasets for Upper Slope and Axis were downloaded in NetCDF format at an averaged temporal resolution of 15-minutes, determined to be adequate for the science objectives of this research. Overlapping coverage of good quality (e.g. minimal data gaps) is primarily during 2013, 2014, 2017, and 2018, and these years were chosen to provide the bulk of the multi-annual analysis, while 2013 will be used as the optimal reference year. Certain comparisons will be possible for other years and seasons, and made when necessary.

For preliminary data management, the primary horizontal velocity datasets were combined in their native NetCDF format, per instrument, and mapped to standard depth bins for ease of analysis. Some physical saturation (e.g. surface layer) and instrument noise at the extreme depth limits of each instrument,

determined from the initial quality checks, result in vertical extrema of -99 to -355 m for Upper Slope data, and -693 to -914 m for Axis data. Though full-depth plots are available, much of the following analysis considers only these depth ranges. NaN values were interpolated using a linear process for gaps less than a day. To deal with larger data gaps, the datasets were subdivided within the NetCDF file and labelled by year and section, then combined using a weighted average as needed.

At Upper Slope, velocity data were rotated using a standard rotation matrix as:

$$u_{rot} = u \cos(\theta) - v \sin(\theta) \quad (4)$$

$$v_{rot} = u \sin(\theta) + v \cos(\theta) \quad (5)$$

where θ is the rotation angle in radians. This was done to better match the cross-slope angle of approximately $+30^\circ$, to help identify relationships between the predominant VICS currents and local slope topography; u is referred to as 'cross-slope', and v is 'along-slope' (Figure 4). At the Axis site, the along-canyon (v) direction is approximately north-south, so no rotation was necessary; u is referred to as cross-canyon.

To deal with the effects of evident stratification, horizontal velocities are WKB-scaled according to:

$$u_{WKB} = (u) \sqrt{\frac{N_0}{N(z)}} \quad (6)$$

and for energy density as:

$$\phi_{WKB} = (\phi) \frac{N_0}{N(z)} \quad (7)$$

with a reference buoyancy frequency of $N_0 = 2.53 \times 10^{-3}$ rad/s based on a reference depth averaged around -900 m (Althaus et al., 2003).

The conductivity-temperature-depth (CTD) climatology data were obtained from the nearby Station LB14, sampled annually May and September during DFO operated La Perouse research cruises, with casts down to -1180 m. Climatology data were used to determine regional water properties, highlighting the stratification variation through depth (Figure 6). From the CTD data, depth-dependent values were obtained for temperature (T), pressure (P), and salinity (S), which were then used to obtain potential temperature (θ), and potential density (ρ_θ) using the UNESCO 1983 (EOS 80) polynomial. The depth-dependent buoyancy frequency was then determined as in Equation 1.

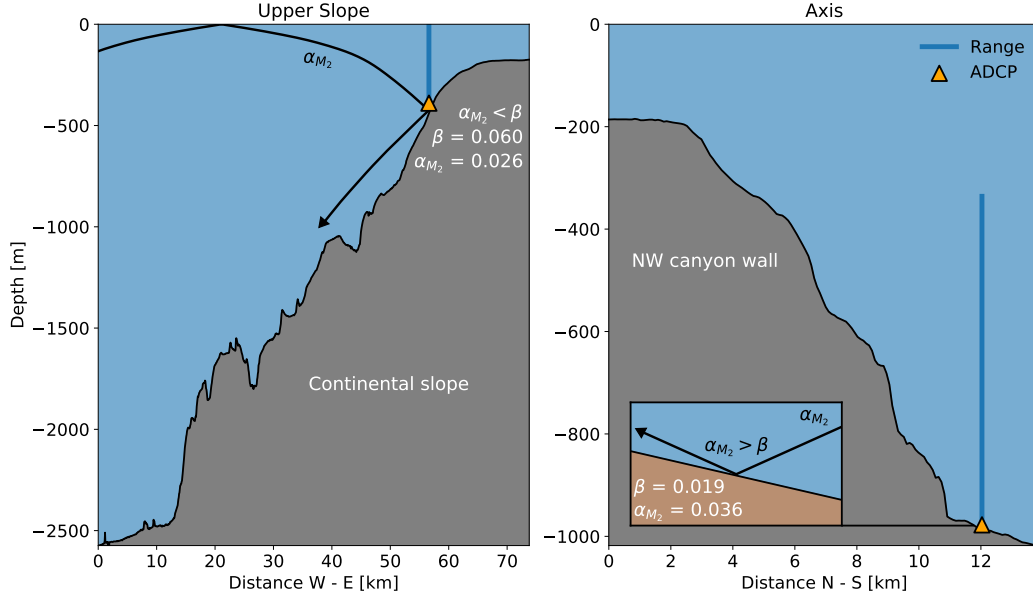


Figure 5: Site topography cross-sections with ray tracing. Local site topography showing the relative locations for Upper Slope (left) and Axis (right) instrument moorings. Horizontal cross-sections were taken in the W-E (left) and N-S (right) directions, represented by the dashed red lines in Figure 4. Horizontal distances range from the shelf to the abyssal plain (left) and canyon floor (right). An incident ray is shown for M_2 , accounting for stratification effects, as well as slope criticality at each site (cite).

Additional supplementary data were obtained from secondary sources as needed. Instrument baseline operational parameters were obtained from Nortek and Teledyne product datasheets. Bathymetry data were obtained from the National Oceanic and Atmospheric Administration (NOAA) National Centre for Environmental Information, as 3 arc-second resolution mean sea level depth. Wind data were obtained from the closest Fisheries and Oceans Canada (DFO) weather buoy, Neah Bay (46206), as time series of magnitude and direction for the comparison years. Surface-level data were obtained from the Canadian Hydrographic Service (CHS) operated gauge in Tofino, nearly directly north of Barkley Canyon, as time series of deviation from chart datum for the comparison years.

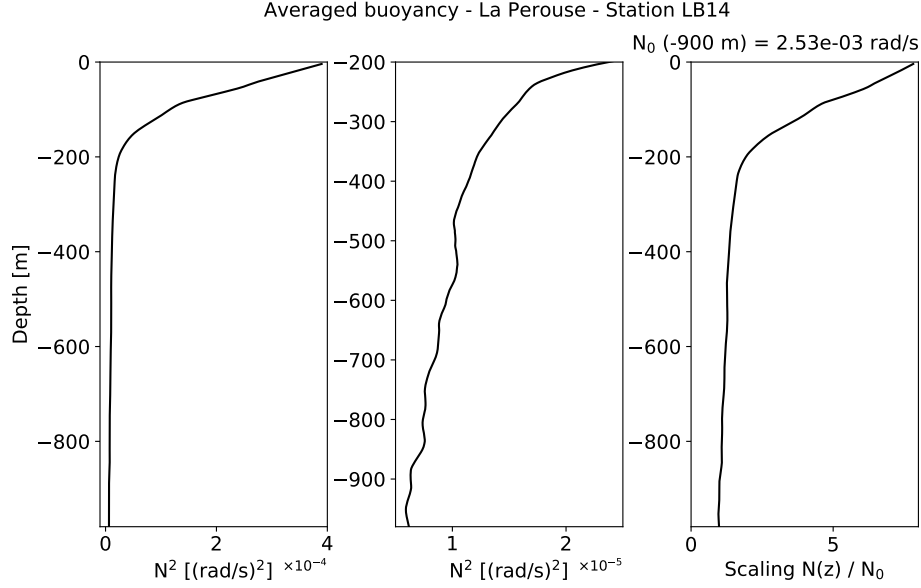


Figure 6: Multi-annual averaged N^2 parameter and WKB-stretch scaling factor. Buoyancy results were obtained as detailed in section 5.1, and are displayed through the water column (left) and below -200 m (centre). A WKB-stretch scaling factor (right) was determined as in Equation 7, based on N_0 averaged around -900 m.

5 Methods

5.1 Frequency spectra

To show the limitations of instrument sampling, the noise floor is the effective lower limit of an instrument for detecting measurement fluctuations, due to inherent noise in an electrical system. In spectral analysis, the noise floor can be thought of as the upper power limit of the inherent noise spectrum, which is equal throughout the frequency domain. To calculate, the standard deviation of the instrument sampling is applied per ping, adjusted as necessary for time-averaged sampling intervals (through standard error of the mean), to determine the total noise variance. This is then applied to the rearranged integral of the noise spectrum, as noise floor level = total noise variance / bandwidth.

Regional water properties were used to determine the local GM internal wave spectrum as it would appear for the open ocean, for comparison with observed spectra. The process was adapted from Callies (2016), using local parameters

$f = 1.73 \times 10^{-5}$ Hz, $g = 9.81(m/s)^2$, and N_0 , along with canonical values for the surface-extrapolated buoyancy frequency (5.24×10^{-3} rad/s), e-folding scale of $N(z)$ (1.3×10^3 m), mode scale number $j^* = 3$, and dimensionless internal wave energy parameter $E = 6.3 \times 10^{-5}$, following from Munk's seminal chapter in Wunsch's *Evolution of Physical Oceanography* (1981).

To better interpret rotation effects, rotary spectra were developed using similar parameters as for PSD, with a more involved spectrogram FFT process based on the work of Gonella (1972), and Thomson and Emery (2014) (Figure 10). To summarise, the adjustment to find the counter-clockwise (CCW) and clockwise (CW) components of a complex horizontal velocity vector, $\mathbf{w}(t) = u(t) + iv(t)$, is the addition or subtraction of the quadrature spectrum, Q_{uv} , as:

$$\text{CCW} = \frac{1}{2}[S_{uu} + S_{vv} + 2Q_{uv}] \quad (8)$$

$$\text{CW} = \frac{1}{2}[S_{uu} + S_{vv} - 2Q_{uv}] \quad (9)$$

where S_{uu} and S_{vv} are the typical complex autospectra used to determine PSD (Thomson & Emery, 2014).

The standard GM spectrum obtained for comparison with PSD was also adapted for rotary spectra. Application of the rotary consistency relation:

$$\frac{\text{CCW}}{\text{CW}} = \frac{(\omega - f)^2}{(\omega + f)^2} \quad (10)$$

to the GM kinetic energy spectrum results in rotary adjusted spectra for both CCW and CW components (Levine, 2002; Polzin & Lvov, 2011).

The PSD and rotary spectrograms described were taken specifically for averaging into those formats, with appropriate resolution to resolve plotted spectral peaks. Spectrograms were 'whitened' by multiplying each power bin by its respective frequency, squared, to better show continuum seasonality. With the intent of observing seasonality, a similar spectrogram FFT process was performed with a window of only 512 data points per segment, resulting in a better temporal resolution of 2.7-day intervals. These were created in both Cartesian and rotary formats. The high-resolution non-whitened broadband spectrogram data were time-averaged for each year to examine frequency depth dependence.

5.2 Critical slope analysis

For observations of free internal waves and tides incident with sloping topography (continental slope, canyon axis and walls, etc.), the angle of the incident

wave, α , and the approximate rise of the topography, β , have a direct relationship. The incident internal wave angle of propagation is evaluated through Equation 11, as:

$$\alpha = \sqrt{\frac{(\omega^2 - f^2)}{(N^2 - \omega^2)}} \quad (11)$$

where ω is the incident wave frequency. To generalise, for $\beta > \alpha$, the slope is considered supercritical and incident waves are reflected back to the open ocean depths; for $\beta \approx \alpha$, the slope is considered critical and the incident waves are amplified; and for $\beta < \alpha$, the slope is considered subcritical and incident waves are scattered up-slope.

To evaluate the local topography, the 2D gradient was calculated from bathymetry measurements and used to determine regions of near-inertial and semidiurnal criticality, as in Figure X.

For the Upper Slope site, specifically, the critical slope angle was separately determined from rise-over-run estimates along a 3 km E-W bathymetry cross-section centred at the ADCP site (Figures 4 and 5), to be $\beta \approx 0.060$, leading to a critical frequency of $\omega_c = 3 \times 10^{-5}$ Hz. This portion of the continental slope is therefore supercritical to internal waves and tides with frequencies below ω_c , reflecting them downward and seaward.

For the Axis site canyon floor (along-canyon slope), the critical slope angle was again separately determined from rise-over-run estimates along a 3 km N-S bathymetry cross-section centred at the ADCP site (Figures 4 and 5), to be $\beta \approx 0.019$, leading to a critical frequency that is sub-inertial. As such, this portion of the canyon floor is subcritical to all freely propagating internal waves and tides, and should scatter incident waves up-canyon. The Axis site canyon walls are difficult to quantify in terms of β , due to highly variable topography, but in general are moderately steep and supercritical to even the semidiurnal constituent. This will be a leading assumption in section 6.5, below.

5.3 Near-inertial slab model

Wind data were analysed for their contribution to near-inertial energy in the mixed-layer, as well as forcing near-inertial internal waves. High temporal-resolution wind data were smoothed using a vector process for both direction and magnitude, to compare generally with seasonal trends and identify forcing. Rotary spectra of u and v components of wind velocity were taken, and integrated over the CW near-inertial band to determine general near-inertial surface wind power.

A slab model analysis was conducted as in D'Asaro (1985) and Alford (2001),

with wind stress calculated as by Garratt (1977) as:

$$\tau_0 = \rho C_D V(z)^2 \quad (12)$$

where ρ is the density of air approximated as 1, $V(z)$ is the complex wind velocity vector, and C_D is the characteristic drag coefficient determined by:

$$C_D \times 10^3 = 0.51 V^{0.46} \quad (13)$$

For appropriate seasonality, a mixed-layer of seasonally varying depth H must be considered, and is defined for the nearby (X km) Line P station 3 as in Thomson and Fine (2003) and Li et al. (2004).

Assuming a null initialisation parameter Z_{I1} at time t_1 , wind generated slab layer near-inertial currents at time t_2 are then computed as:

$$Z_{I2} = Z_{I1} e^{-\omega \Delta t} - \frac{T_t}{H \omega^2} (1 - e^{-\omega \Delta t}) \quad (14)$$

where a damped rotation frequency, ω , is determined as:

$$\omega = r + i f \quad (15)$$

with $r = 0.15f$ as an artificial damping parameter, set as in Alford (2001); and

$$T_t = \Delta T / \Delta t \quad (16)$$

is related to the complex stress vector defined as:

$$T = \frac{\tau_x + i \tau_y}{\rho_{ML}} \quad (17)$$

where $\rho_{ML} = 1024 \text{ kg/m}^3$ is the average density of the mixed-layer.

The near-inertial flux by the wind into the mixed layer at time t_2 is then computed as:

$$\Pi = \text{Re} \left\{ \frac{T_t^*}{\Delta t |\omega|^2 H} \left[\left(Z_{I1} + \frac{T_t}{\omega^2 H} \right) (e^{-\omega \Delta t} - 1) + \frac{T_t}{\omega H} \Delta t \right] \right\} \quad (18)$$

To identify possible generation of near-inertial internal waves at the base of the mixed-layer, a 'pumping' model is added to the above slab model process.

5.4 Dissipation estimates

Internal wave interaction theory description.

6 Results

6.1 Mean currents

Observations:

Regional mean currents are topographically guided, and show little inter-annual variation (Figure X - low-pass vel plots for each year (appendix?)). To identify mean currents in the horizontal velocity data, a 40-hour, 8th-order, digital low-pass Butterworth filter was applied in both directions. At Upper Slope, they are as expected for this region (Thomson et al., etc.), being mostly poleward along-slope with a sharp shift to upwelling-favourable equatorward flow in the late-spring, through depth (Figure 7). The poleward currents then push back to the surface over the course of the summer. Deeper currents are somewhat stronger near the slope (about 0.2 m/s) versus the surface (about 0.1 m/s). In the canyon, mean currents are prominently along-canyon, mostly towards the canyon head, with no apparent seasonality or depth-dependence (Figure 7). They are much weaker in the canyon than on the slope, at about 0.04 m/s.

Mean currents comparisons.

Brief mean currents speculation.

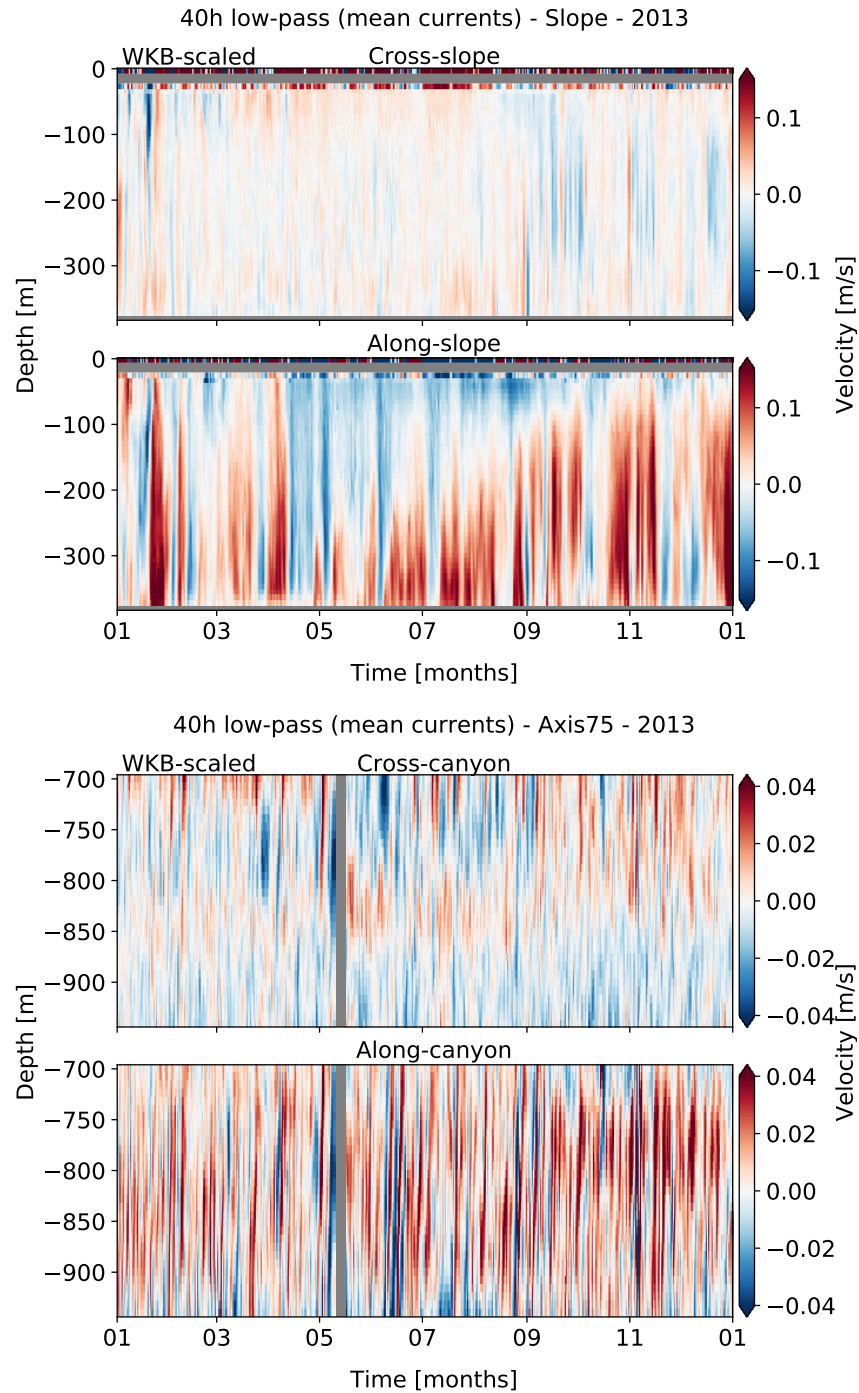


Figure 7: 40-hour low-pass horizontal velocity data for Upper Slope (top) and Axis (bottom), in 2013. For each, components are separated as cross- (upper) and along-slope/canyon (lower). Velocities are 'adjusted', in that they have been rotated and NaN-interpolated, as detailed in section 4. Intensity has been scaled for clear visual representation of current trends.

6.2 Tidal currents and internal waves

Observations:

A two-week snapshot of the 40-hour high-pass velocities during the recurring May mean-current switch (here in 2013) shows the presence of internal waves and tides of different frequencies and vertical structure (Figure 8). At the Upper Slope site, high-pass currents reach up to about 0.1 m/s in both cross- and along-slope directions, most strongly in the bottom 150 m, with some non-uniform structure above -250 m depth, and no apparent seasonality. At Axis, high-pass currents are strongest in the bottom 250 m (up to about 0.2 m/s) and dominantly along-canyon, with fairly uniform vertical structure through depth, and no apparent seasonality (Figure 8).

****CHANGE FIGURE TO MAY****

High-pass velocity comparisons.

Brief high-pass velocity speculation.

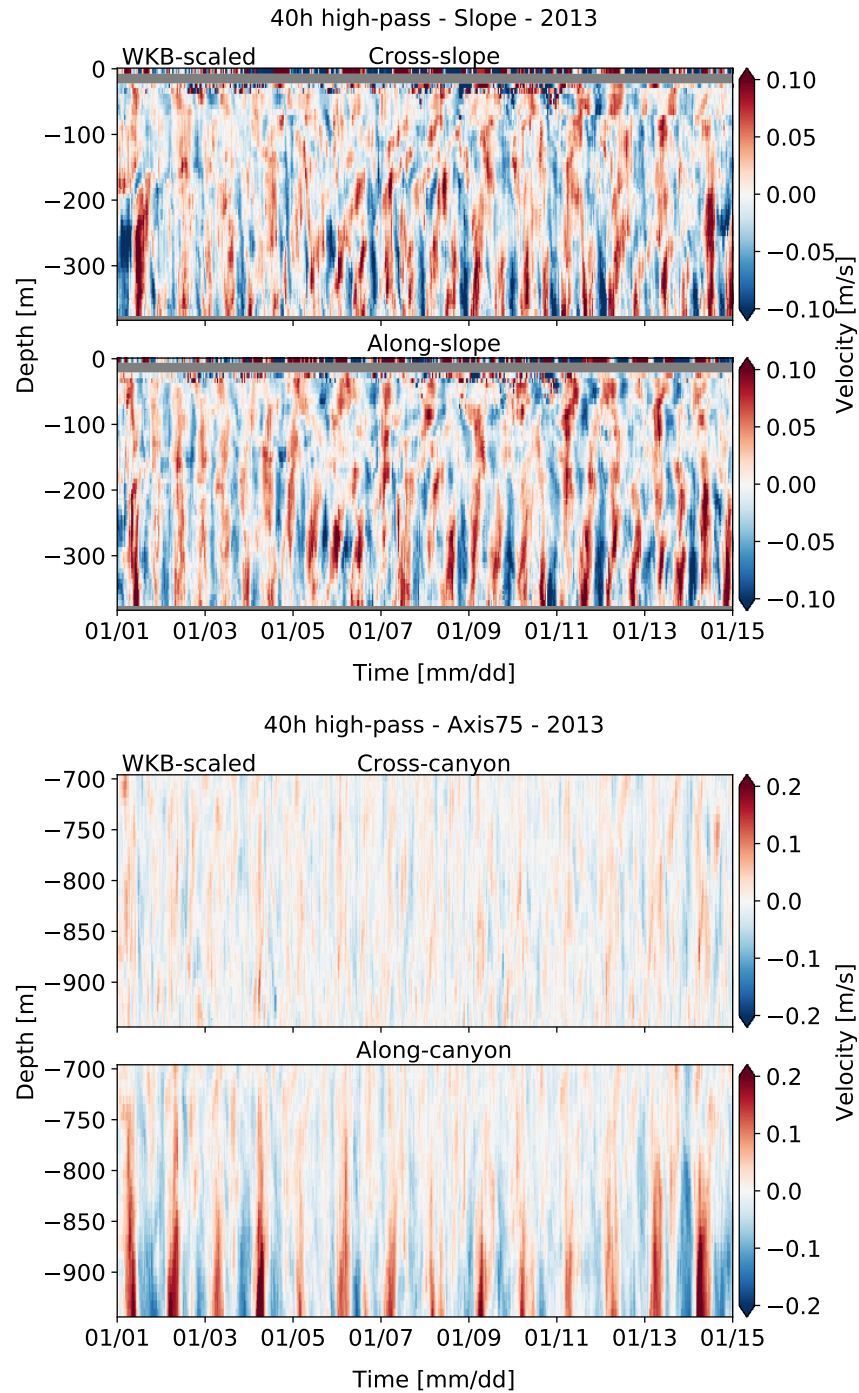


Figure 8: 40-hour high-pass horizontal velocity data for Upper Slope (top) and Axis (bottom), in April 2013. For each, components are separated as cross- (upper) and along-slope/canyon (lower). Velocities are 'adjusted', in that they have been rotated and NaN-interpolated, as detailed in section 4. Intensity has been scaled for clear visual representation of current trends.

6.3 Frequency response

Observations:

Spectra for both sites show strong tidal and near-inertial influence, as well as little inter-annual variability (Figures 9 and 10). The primary tidal constituents present at Barkley Canyon are of the diurnal (once-per-day) and semidiurnal (twice-per-day) frequencies. Their induced regional currents, along with the near-inertial flows associated with the Coriolis parameter, f , dominate the spectra and observed motions. In annual power spectra at Upper Slope, the strength of the diurnal peak is equivalent to the wind-driven near-inertial f peak (about $2 \times 10^2 \text{ (m/s)}^2/\text{Hz}$), and half the strength of the semidiurnal (about $5 \times 10^2 \text{ (m/s)}^2/\text{Hz}$), as expected from previous observations of tidal constituents on the VICS (Thomson et al., 1990; Allen et al., 2001). The extreme low-frequency range, or subdiurnal (below about $5 \times 10^{-6} \text{ Hz}$), is similarly strong and more of a continuum than a peak. At the opposite end, the high-frequency internal wave continuum above the M_4 sum peak diminishes with close to the expected -2 roll-off for the open-ocean GM internal wave spectrum (as discussed in section 6.8), and at both sites there are elevated continuum levels.

Frequency comparisons.

Frequency speculation.

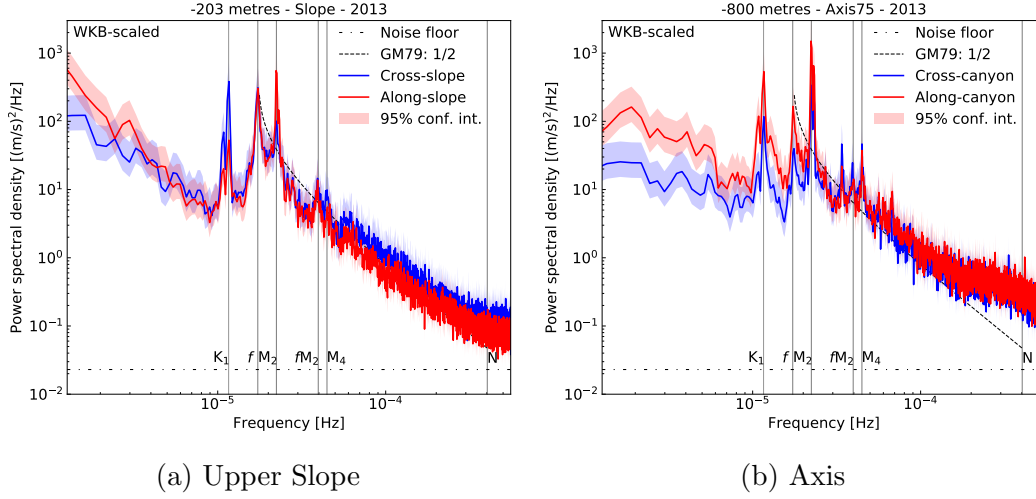


Figure 9: Time-mean PSD for (a) Upper Slope and (b) Axis in 2013, from adjusted horizontal velocity data. Both cross- (blue) and along-slope/canyon (red) components are shown for comparison, with 95% confidence intervals. For reference, the instrument noise floor (dotted line), component-wise GM79 spectrum (dashed line), and key frequency constituents (vertical lines) are shown.

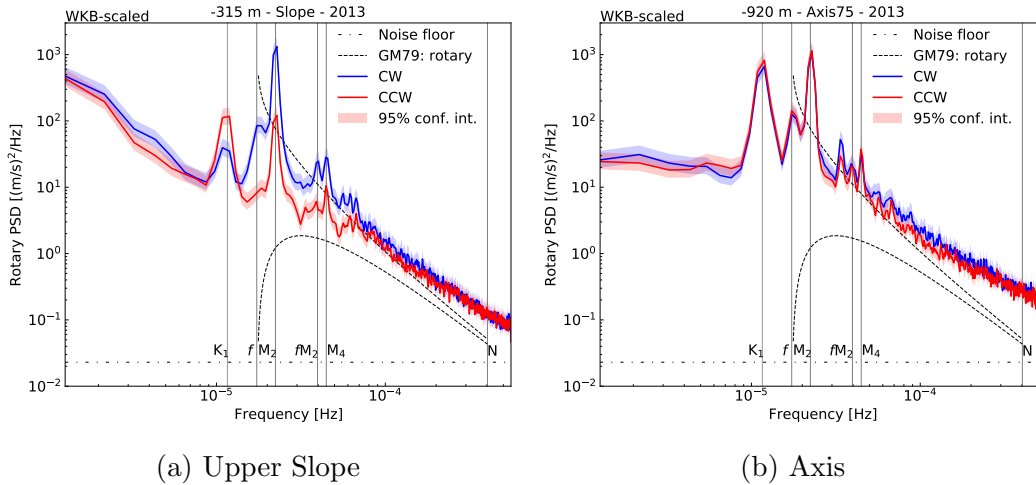


Figure 10: Time-mean rotary spectra for (a) Upper Slope and (b) Axis in 2013, from adjusted horizontal velocity data. Both CW (blue) and CCW (red) components are shown for comparison, with 95% confidence intervals. For reference, the instrument noise floor (dotted line), rotary GM79 spectrum (dashed lines), and key frequency constituents (vertical lines) are shown.

6.4 Slope effects

Observations:

The depth dependence of each frequency band is notably affected by proximity to topography. For Upper Slope, this is evident in changes to direction and rotation, and the seasonally variable intensification of a thick (~ 150 m) layer directly above the slope.

To identify depth-dependence, prominent frequency constituents were integrated over a bandwidth estimated to encompass the majority of the respective spectral peak or continuum, as subdiurnal (x-x Hz), diurnal (x-x Hz), near-inertial (x-x Hz), semidiurnal (x-x Hz), and the internal wave 'continuum' (x-x Hz). This was performed for each depth bin along consecutive time steps, the output resulting in 'depth-band integrated power' spectra.

In the upper depths (above -250 m) there appears to be little influence from the slope. All bands experience prominently CW motions, as expected due to rotation effects in the northern hemisphere. Furthermore, all bands experience close to equal distribution between cross- and along-slope directionality. When observing non-WKB-stretch scaled spectra, there is obvious near-surface intensification (Figure X).

Below about -250 m topographic effects arise and increase with proximity to the bottom. All bands, excluding the near-inertial, show near-slope intensification of $1\times$ to over $2\times$ orders of magnitude; the near-inertial band shows annuation of a similar magnitude. The subdiurnal and diurnal bands show strong intensification in the CCW rotary component (about $1.5\times$ orders of magnitude). The semidiurnal (about $2\times$ orders of magnitude) and continuum (about $1\times$ orders of magnitude) bands show CW intensification. The subdiurnal and diurnal intensification is mostly in the along-slope direction, while the semidiurnal and continuum bands both see a close to equal distribution between the cross- and along-slope components, similar to how they are distributed in the upper depths. Furthermore, the near-inertial band shows the mentioned attenuation in the CW component (which is dominant), with proximity to the slope. The other bands show no weakening effects; their intensified components simply rise to meet or overtake those dominant in the upper depths. All bands are affected over a similar vertical scale of approximately 150 m above bottom (AB), up to 200 m AB during pulses of intensity.

(Depth-frequency plots.)

Discuss criticality of slope topography.

Comparisons:

Continental slopes are common study sites, and their irregular geometry is known to have significant effects on both incident and locally generated internal waves and tides. Intensified near-slope layers are prevalent in the literature, noted in similar cases by Kunze et al. (2012), Nash et al. (2004), and Polzin et al. (1997). Similar results are traceable back to a seminal study by Hotchkiss and Wunsch, in 1982, who found a $\sim 10\times$ increase in near-slope internal wave energy near Hudson Canyon, with a depth-dependent vertical scale of about 150 m AB at -400 m depth. More recently, Robertson et al. (2017) found that where criticality (β/α , as detailed in section 5.2) is near to 1, typically below the shelf-break and along the upper slope, diurnal and semidiurnal internal tides were most strongly subject to near-slope enhancement. Xie and Chen (2021) found further evidence of near-critical bottom-enhancement of diurnal and semidiurnal internal tides exceeding 150 m AB, in the South China Sea.

For Barkley Canyon and the nearby slope, the diurnal constituent is sub-inertial, so it is unlikely for there to be incident diurnal internal tides from the open ocean. At slopes along the California Current System, Johnston and Rudnick (2015) found that generated sub-inertial diurnal internal tides were evanescent (trapped) to slope topography poleward of their turning latitude ($\sim 30^\circ\text{N}$), but could still propagate alongshore. Robertson et al. (2017) found further evidence of trapped diurnal internal tides at Barcoo seamount, north of their turning latitude, where generated diurnal currents were strong along-slope but could not propagate away from the supercritical topography. On the VICS, Cummins and Oey (1997) found that diurnal internal tide generation was prevalent at the continental slope, and that motions were trapped along-slope unable to radiate offshore.

For near-inertial internal waves, which are generated by wind at the ocean surface and propagate downward, Thomson et al. (1990) found that as they approach a slope they become somewhat attenuated as they are absorbed by increased vertical shear in the background flow, associated with topographically trapped oscillations.

In terms of the semidiurnal band, Terker et al. (2014) found evidence of near-bottom elevated energy-flux associated with semidiurnal internal tide generation on the continental slope near Monterey Bay, with a vertical scale of about 200 m AB in similar depths to the Upper Slope site. Marques et al. (2020) found further evidence of bottom-enhanced semidiurnal energy at a supercritical slope near Tasmania, of up to $10\times$ intensification. Off the west coast of India, Subeesh et al. (2021) found that for sites offshore of the shelf-break generation zone, propagation for the baroclinic semidiurnal tide is downward; furthermore, the supercritical upper slope prevents much of the incident off-

shore semidiurnal internal tides from propagating onto the shelf, as they're reflected back to the open ocean, again downward. Drakopoulos and Marsden (1993) found that for the Vancouver Island continental margin, seaward of the shelf break, that the semidiurnal internal tide propagation was strongly CW and downward. Xie and Chen (2021) noted that for obliquely incident internal waves and tides, generated near-slope currents are in the direction of incident wave propagation, and so should continue to follow the downward trend on the slope.

Continuum comparisons.

Speculation (MOVE SOME OF THIS TO DISCUSSION):

The instrument location below the VICS shelf-break (Figure 5), at a depth of -378 m, suggests that this depth dependence is related to the effects of the supercritical upper continental slope on incident and locally generated internal waves and tides.

At Barkley Canyon, the 'rubbing' of the barotropic diurnal tide along the slope should still produce diurnal internal tides; however, these would be trapped radiating upward (CCW) near to the topography in a concentrated layer, only able to really propagate in the along-slope direction, as observed. Additionally, poleward propagation of free baroclinic CTW of diurnal frequency from the mouth of the nearby Strait of Juan de Fuca may contribute to the observed along-slope currents, though this is debatable as their strength should diminish with depth beyond the shelf-break (Thomson et al., 1982; Kuroda et al., 2018). These same effects could also apply to the subdiurnal band, being similarly sub-inertial, with forcing at such low frequencies possibly being due to regional mean currents.

Since the Upper Slope site is supercritical ($\beta \approx 0.060$) to near-inertial frequencies ($\alpha \approx 0.023$), the CW reduction near-bottom is as expected. It is further possible that downward propagating near-inertial internal waves that are not entirely attenuated are then reflected downward, maintaining some presence in the lower layer. Furthermore, the intensification in this band should be minimal compared to what is observed for the semidiurnal constituent, consistent with a relatively weak near-inertial criticality parameter ($\beta/\alpha \approx 2.6$) at this site. Indeed, intensification in the near-inertial band is barely evident.

As the Upper Slope site is supercritical to the semidiurnal constituent ($\alpha \approx 0.037$), any incident semidiurnal internal tides should be reflected downward, as is suggested by the strong CW intensification observed. Additionally, a stronger criticality parameter ($\beta/\alpha \approx 1.6$) suggests focusing of semidiurnal

waves to a greater degree than for the near-inertial or continuum bands, also evident in the observations. Finally, the semidiurnal intensified signal is nearly equally distributed between cross- and along-slope components, similar to its state in the upper depths.

Intensification in the super-tidal internal wave continuum is more subtle. As the band is broad, much of it is far from being near-critical, so intensification is weaker than for other constituents such as the semidiurnal, as expected. Although the background state of the band appears to trend slightly towards the cross-slope and CW components, intensification seems to apply somewhat equally to all components; everything intensifies by a factor of about $1 \times$ order of magnitude. Besides the entirety of this band being less energetic than the tidal and near-inertial constituents, it is possible that the (relatively) small-scale motions characterised by these higher frequencies act to reduce the scale of the near-slope effects. - Wunsch chapter 2 'critical layers' to finish this paragraph.

6.5 Canyon effects

Observations:

For Axis, as at Upper Slope, notable frequency constituents show depth dependence due to proximity to topography. This is similarly evident in changes to both direction and rotation, and seasonally variable intensification in a thick (~ 250 m) layer above the narrow canyon bottom.

Nearly all frequency bands (besides the continuum) display rectilinear, intensified along-canyon flow below ~ 750 m, with near-topography integrated power peaking at approximately $\sim 5 \times 10^{-3} \text{ (m/s)}^2$ (a near-bottom intensification of up to $3 \times$ orders of magnitude). Inter-annual variability is minimal. Both the subdiurnal and diurnal bands are entirely along-canyon, with little to no power in the cross-canyon direction. The near-inertial band is also almost entirely along-canyon, with only the strongest pulses showing up weakly ($\sim 7 \times 10^{-4} \text{ (m/s)}^2$) in the cross-canyon component. The semidiurnal band is strongly along-canyon, but with a medium-strength ($\sim 1 \times 10^{-3} \text{ (m/s)}^2$) cross-canyon signal that is sharply attenuated about 100 m AB. The continuum differs in that it is fairly weak ($\sim 4 \times 10^{-4} \text{ (m/s)}^2$), prominently CW and in both cross- and along-slope directions, with cross-slope power being slightly greater.

(Reference Appendix A for plots).

Discuss criticality of canyon bottom (subcritical) and walls (supercritical).

(Plots of near-inertial and semidiurnal criticality).

Comparisons:

Speculation:

The Axis instrument site is deep, at a narrow turn mid-way along the length of the canyon bottom. Any low frequency incident waves entering the canyon are likely to be reflected downward by the supercritical walls, or scattered up-canyon by the subcritical floor. Locally generated semidiurnal and near-inertial waves from along-canyon currents could be forced by oscillations at the canyon mouth, only to suffer the same reflection and scattering; while the sub-inertial diurnal internal tides would once again be trapped to the canyon floor and walls, dissipating locally. These effects, along with simple increased stratification near topography, could compound into the near-bottom intensification that is present. Additionally, the cross-slope motions that are progressively evident in higher frequency bands are likely associated with the smaller wavelengths of the generated or incident waves. Incident cross-canyon semidiurnal internal tides can likely only get so deep before potential dissipation, while small-scale high-frequency internal waves would be less affected by the tight canyon, and could propagate in both cross- and along-slope directions.

6.6 Subdiurnal & tidal seasonality

Subdiurnal seasonality is lacking in the canyon, and on the slope only shows up in subtle pulses in the winter and fall.

(Subdiurnal depth-band plots.)

Diurnal seasonality shows a pulse in the late-spring/early-summer, and a smaller pulse in the late-fall/early-winter, obvious at Slope and somewhat evident at Axis.

(Diurnal depth-band plots.)

For seasonality comparisons, barotropic tidal data were obtained from sea-surface level measurements, and their power spectra band-pass filtered to compare with the depth-mean component of the depth-band integrated power spectrograms.

Diurnal barotropic forcing is consistently in-phase, with low or null lag correlations, and a scaled depth-mean of similar amplitudes, at both sites. Suggests local barotropic forcing.

(Diurnal barotropic plots.)

Diurnal comparisons.

Semidiurnal seasonality is similar to the diurnal at Slope, and appears to be absent (temporally uniform intensification) at Axis.

(Semidiurnal depth-band plots.)

Semidiurnal barotropic forcing is in-and-out of phase at both sites, though the 'in-phase' segments may be coincidental remote forcing; and scaled amplitudes vary greatly from the barotropic surface tide. Large visual offsets appear in the winter, spring, and fall; an average of five largest offsets at Slope in 2013 winter/spring (Jan - April) is 80.9 hours or 3.37 days. Similar offsets are observed at Axis in 2013, and are repeated each year. Average of all years and sites about 86 ± 12 hours, due to coarse time resolution of the depth-mean time series. To generalise, the offset is 3 - 4 days.

This is confirmed through 4-month phase lag correlations, with time segments of months 1-4, 5-8, and 9-12. Phase lag is consistent at a minimum of $X \pi$, with months 5-8 showing an increase associated with greater amplitudes at this time.

(Semidiurnal barotropic comparison plots, 2013).

(Semidiurnal barotropic offsets plots, spring/winter 2013).

Regional mode 1 wave speed c_1 (Chelton, 1998) is between 2.0 - 2.4 m/s (average 2.2 m/s), depending on distance from Vancouver Island, with minimal seasonal variation below the mixed layer. For the generalised offsets determined, this suggests a travel distance of 700 - 800 km.

(Semidiurnal barotropic plots.)

Semidiurnal comparisons. Drakopoulos and Marsden (1993) found that the semidiurnal internal tide field on the continental margin off of Vancouver Island gained strength in the late-spring through summer, and attenuated by September, associated with seasonal changes in stratification.

Brief forcing speculation. Subdiurnal seasonality is subtle, but does recur annually, and could be linked to storms and/or seasonal changes in stratification but it is difficult to make any substantial correlation. Diurnal seasonality is more obvious, and Cummins (2000) associates strengthened diurnal tidal flow over the VICs with summertime increased stratification. In addition to seasonal stratification variability and storms, the timing of the late-spring/summer pulse aligns with the annual switch to upwelling-favourable equatorward currents along the Slope, driving along-canyon flow, suggesting diurnal interaction with regional mean circulation (Crawford and Thomson, 1984) at both sites. It is likely that similar effects may be driving the semid-

urnal seasonality on the Slope, but this does not fit well with the lack of semidiurnal seasonality in the canyon.

In terms of tidal forcing, the phase timing and scaled amplitudes of the depth-mean diurnal signal coincides well with the local barotropic, while the semidiurnal timing offsets suggest that remotely generated incident semidiurnal internal tides are likely present. If so, there numerous potential sources. They could originate from somewhere along the Juan de Fuca Ridge (Arbic et al., 2012; Carerre et al., 2021), as the main open-ocean geological features in range. The closest segments of the Juan de Fuca Ridge are about 400 - 600 km away (2 - 3 days, assuming average c_1 of 2.2 m/s (Chelton, 1998)), depending on the segment. However, the observed average phase offset suggests incident waves from 700 - 800 km; the Juan de Fuca Ridge is potentially too near. The Haida Gwaii islands to the northwest are also known to generate semidiurnal internal tides (Cummins and Oey, 1997; Arbic et al., 2012; Li and Stortch, 2020), and are in range at around 600 - 800 km distant, however, the internal tides would have to propagate over the VICs to reach Barkley Canyon, likely dissipating much of their energy along the way. As such, the most likely source of remotely generated semidiurnal internal tides is Mendocino Escarpment, one of the strongest regional generation sites for mode-1 and mode-2 semidiurnal internal tides (Althaus et al., 2003; Arbic et al., 2012; Zhao, 2017; Morozov, 2018). Strong northward propagating mode 1 internal tides, along with its location about 800 km to the south of Barkley Canyon (4 days), fit well with the observed phase lag.

6.7 Near-inertial seasonality

Near-inertial seasonality is highly intermittent, most evident in the fall and winter, with major events year round at Slope, but only significant events in the fall and winter showing up at Axis.

(Near-inertial depth-band plots.)

Slab model results show significant mixed-layer currents and positive flux as a result of specific wind events (size, rotation, etc. are important) and seasonal mixed-layer depth. These are most obvious in the fall and early winter.

(Near-inertial slab currents and flux plots.)

Near-inertial wind contributions to the slab layer are not correlated with internal wave observations, though timings are visually related.

(Near-inertial wind correlation plots.)

To relate the slab model response to near-inertial internal wave generation,

beneath, a further 'pumping' model is considered...

Near-inertial comparisons.

Brief near-inertial speculation. Near-inertial internal waves occur when surface winds excite currents in the mixed layer that 'pump' energy into the internal wave field, below. Due to the restricted nature of free internal waves, these near-inertial internal waves propagate downward and equatorward until they interact with topography or mesoscale flows, or refract. It is important to note that not all wind events produce similar inertial input, e.g. fairly linear trade winds versus a rotating low pressure system. Small storms with significant rotation are the leading source of the highly intermittent input, and occur most often in the late-fall and winter; small cold fronts and lows can induce greater inertial currents than synoptic scale storms, and it is the CW near-inertial frequency component of the wind that contributes the most energy to the mixed-layer. Intensity of the wind generated mixed layer currents is further associated with the seasonal mixed-layer depth, which shifts the seasonal inertial input peak towards October for the Northern Hemisphere, when the mixed layer is still thin and storms are prevalent. The response of the mixed layer may then generate near-inertial internal waves through a 'pumping' mechanism at its base... (Garratt, 1977; D'Asaro, 1985; Alford, 2001; Thomson and Fine, 2003; Li et al., 2004; Voelker et al., 2020)

6.8 Continuum seasonality

Continuum seasonality on the slope is similar to the diurnal and semidiurnal, with the most notable features being a pulse in the late spring and a lull in the late summer.

Continuum seasonality in the canyon is similar to the near-inertial band, with only the fall pulses showing up at Axis.

(Continuum depth-band plots.)

From PSD calculated through depth, the continuum was further evaluated for seasonal variability. The frequency range of 7×10^{-5} Hz to 2×10^{-4} Hz is here defined as the internal wave 'continuum', with bandwidth greater than the M_4 spectral sum peak and less than the local depth-average buoyancy frequency. For each 2048 point Hanning window with 50% overlap, a power law of af^b was fit to the continuum. However, the a and b time series were found to be highly variable, while b was expected to be fairly close to the canonical GM slope of -2, and so were compared to the individual spectra to evaluate fit accuracy. The results...

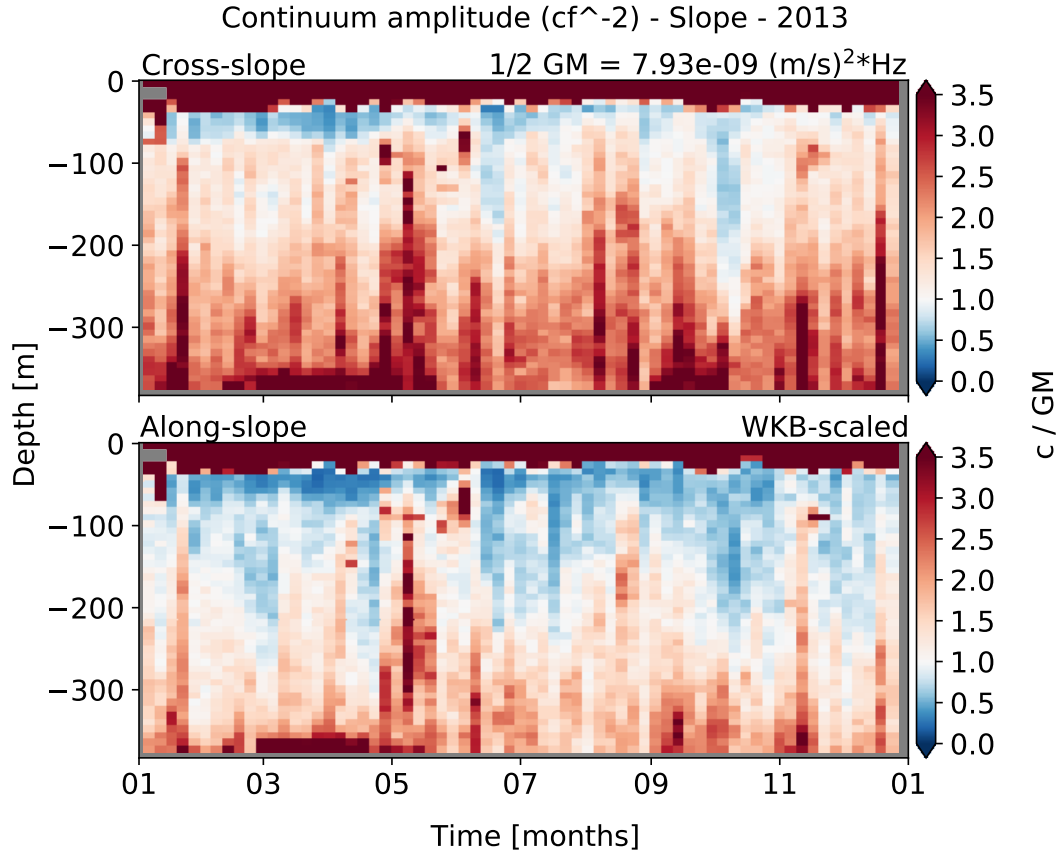


Figure 11: Continuum amplitude (c) versus GM amplitude over the same frequency range, for Upper Slope in 2013. Results are obtained from WKB scaled spectra.

(Time series of a and b power law variables.)

To more consistently compare continuum amplitudes, each power bin of the continuum band was 'whitened', multiplied by its corresponding frequency, squared, and the band average value determined. This was compared at each window and depth bin against a value for the $1/2$ GM continuum range of $7.93 \times 10^{-9} (\text{m/s})^2 \times \text{Hz}$, determined by the same method. The variability evident in the results is remarkably similar to the integrated depth-band power observations for the continuum, with c/GM values reaching $3.5\times$ at Slope, and $6\times$ at Axis, at times and depths coinciding with enhanced power.

The amplitude fits were then used to make general estimations of internal

wave forced dissipation rates, D , on the slope and in the canyon. Dissipation rates were estimated based on internal wave interaction theory, as described in Section 5.4. Results are...

(Dissipation plots.)

Continuum analysis comparisons.

Brief continuum speculation.

7 Discussion

It was found that inter-annual variability is largely absent, at both sites. Seasonal regional mean currents exist along the slope, as expected, while the canyon shows little seasonal variability. High-pass velocities show internal waves and tides with some vertical structure, at Upper Slope, and uniform vertical structure at Axis. Both mean and high-pass currents show subtle indications of bottom enhanced currents. The diurnal, semidiurnal, and near-inertial frequency constituents dominate the local spectra, as expected, and the high-frequency internal wave 'continuum' shows a roll-off near to the expected -2 slope for GM open-ocean internal waves, albeit with heightened variance. Subdiurnal, tidal, and continuum bands show seasonal near-slope enhancement, while the near-inertial band is attenuated near the bottom. In the canyon, all frequency bands show near-bottom enhancement. Seasonality for the subdiurnal band is weak at both sites. The diurnal band shows pulses in the late-spring and fall, mostly at Upper Slope in the along-slope direction. The semidiurnal band shows similar seasonality at Upper Slope, which does not appear at Axis. The near-inertial band shows sporadic pulses of power that are prominent in the spring and fall on the slope, with only some of the fall and early-winter events showing up in the canyon. The continuum shows seasonal pulses that occur mostly in the fall, at both sites, and generally elevated variance as compared to GM.

The WKB-stretch scaling largely removes near-surface effects, so a connection to stratification is obvious. However, the WKB-stretch scaling is based on deep CTD casts that were made nearby, but away from topography; the stratification profile captures the surface mixed-layer, but does not adjust for possible stratification effects near the slope or in the canyon (Figure 6). Hotchkiss and Wunsch (1982) noted increased stratification effects near areas of high 'topographic relief', such as the shelf-break and slopes. These highly stratified turbulent layers experience the effects of reflection, scattering, and internal tide and lee-wave generation, as well as amplification of internal waves and

tides, in general. Further research would benefit from site specific climatology data.

Expanded possible explanations and connections (where necessary).

Speculation.

(Supplemental figure.)

Sources of error and improvements.

Potential for future research.

8 Conclusions

Internal waves and tides drive mixing processes, and contribute to local productivity, regional transport of nutrients, heat, and momentum, and the large-scale overturning circulation and climate. Irregular topography such as submarine canyons and continental slopes can focus internal waves and lead to breaking events, instigation fine-scale dissipation that drives these processes. As such, a better understanding of internal wave interactions with irregular topography is important for management of fisheries, pollution, and climate modelling.

Four years of ONC managed horizontal velocity data from Barkley Canyon, at both canyon and slope sites, allowed for investigation into the local internal wave field. Velocity data were evaluated in both time and frequency domains using digital filtering and various power spectra processes.

It was found that inter-annual variability is largely absent, at both sites, and that seasonal mean currents on the slope are as expected for this region. Canyon seasonal variation is minimal, and flows are mostly along-canyon. Typical tidal and near-inertial frequencies dominate the spectra, and there is depth-dependence in each band associated with topographic effects. There is unique seasonal dependence for frequency constituents, and the internal wave 'continuum' shows heightened variance and flattened slope as compared to the GM open-ocean model.

Results could be improved through the use of site specific climatology, sampling consistency between instruments, additional instruments across topography, and more overlapping comparison years between sites. It would be interesting to evaluate the observed trends on a decadal scale, and potentially observe the effects of changing climate on local water properties and processes.

Barkley Canyon is a dynamic submarine region which physical processes that

show unique spatial and temporal characteristics. As canyons and slopes are known to contribute significantly to local productivity and even large-scale climate effects, ONC's Neptune cabled observatory is an exciting network for uncovering the hidden stories of the continental margin. The accessibility of publicly available data in this region designates Barkley Canyon as a key observational laboratory for furthering ocean research, and connecting scientists and communities in the sharing of knowledge.

9 Appendix A: Inter-annual

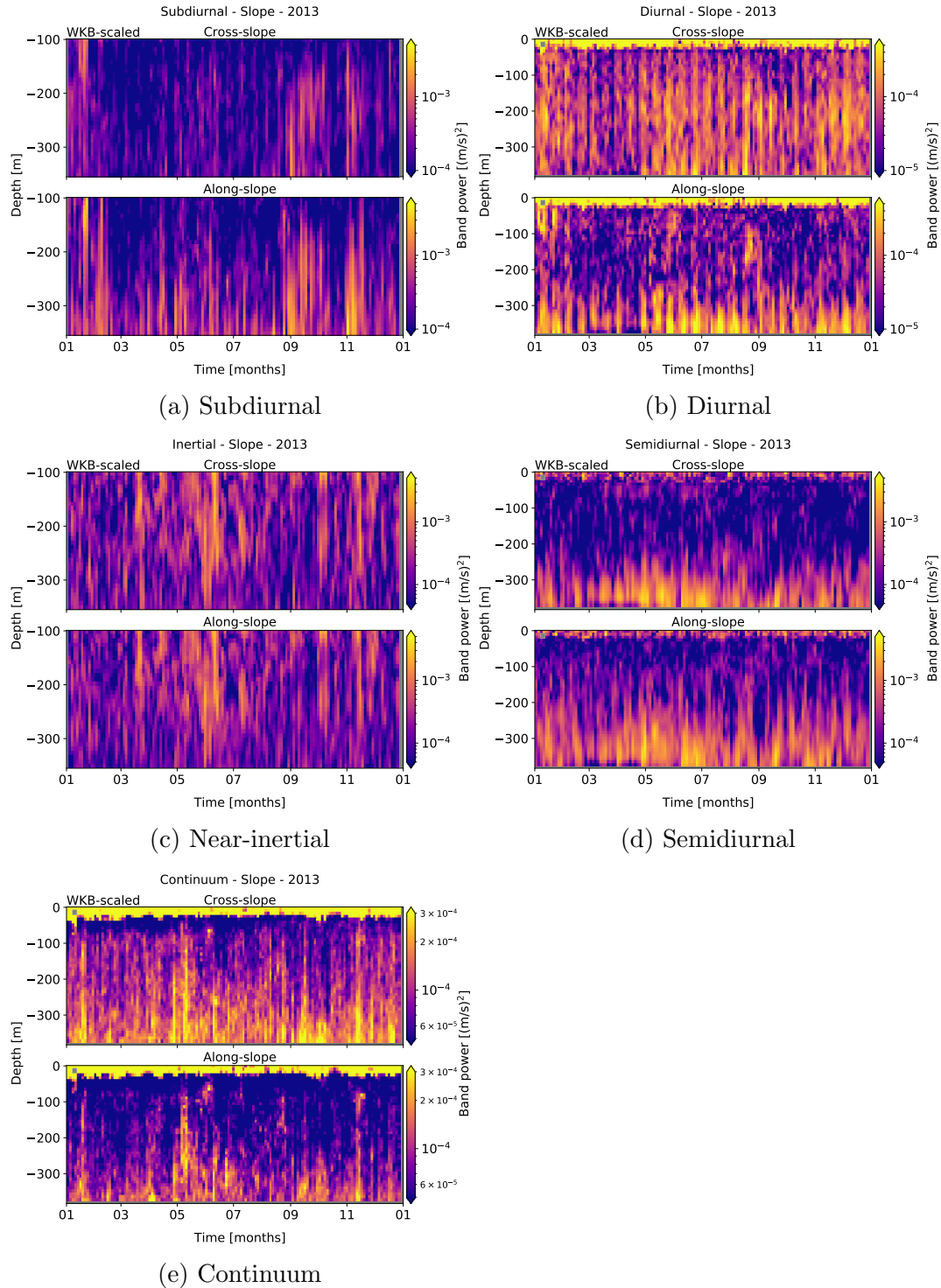


Figure 12: Band-integrated PSD data for Upper Slope in 2013, for rotated, cleaned, and WKB-scaled horizontal velocity data. For each sub-figure, there are cross- (top) and along-slope (bottom) components. Intensity scales are adjusted for visual clarity of effects.

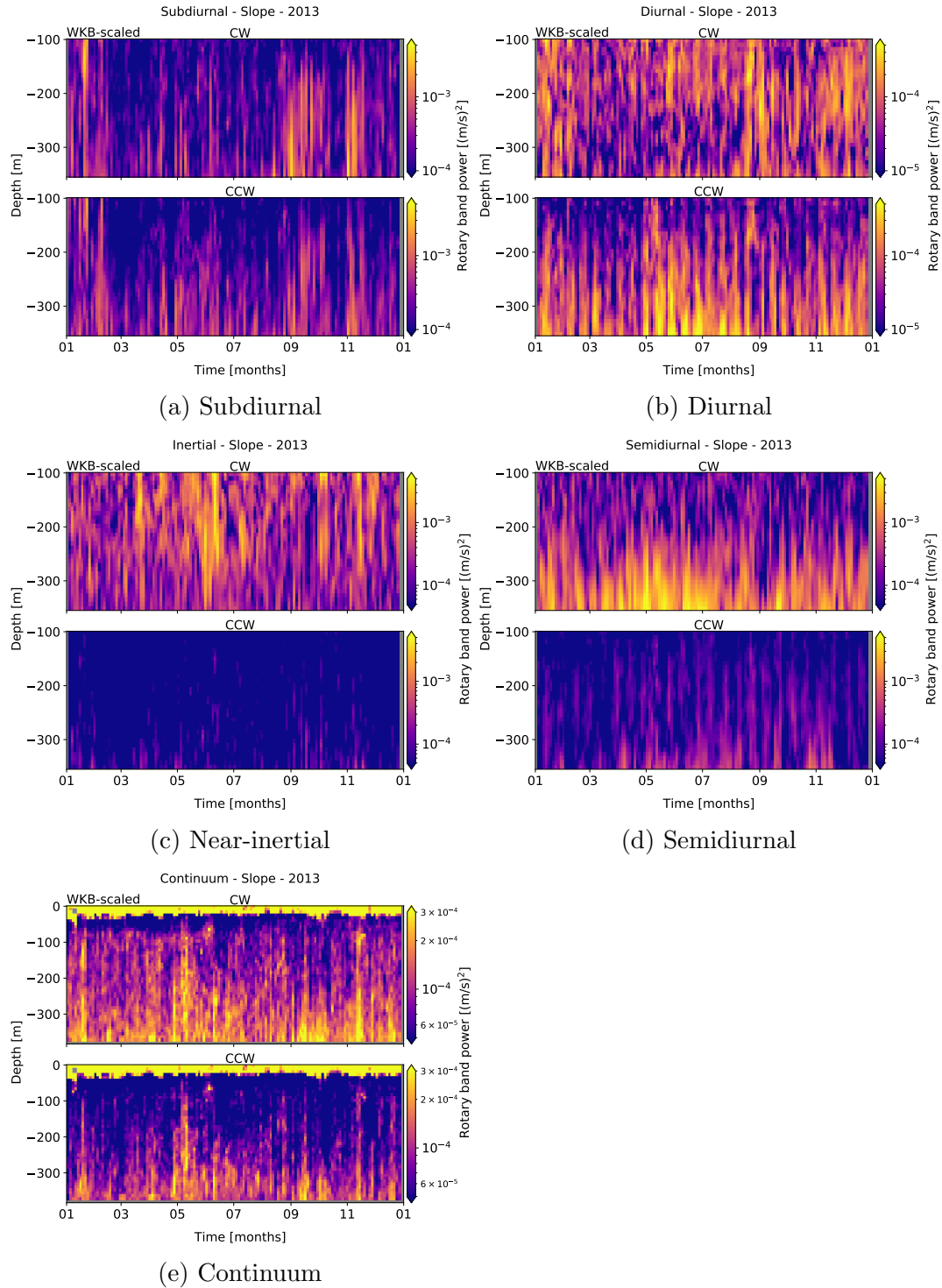


Figure 13: Band-integrated rotary data for Upper Slope in 2013, for rotated, cleaned, and WKB-scaled horizontal velocity data. For each sub-figure, there are CW (top) and CCW (bottom) components. Intensity scales are adjusted for visual clarity of effects.

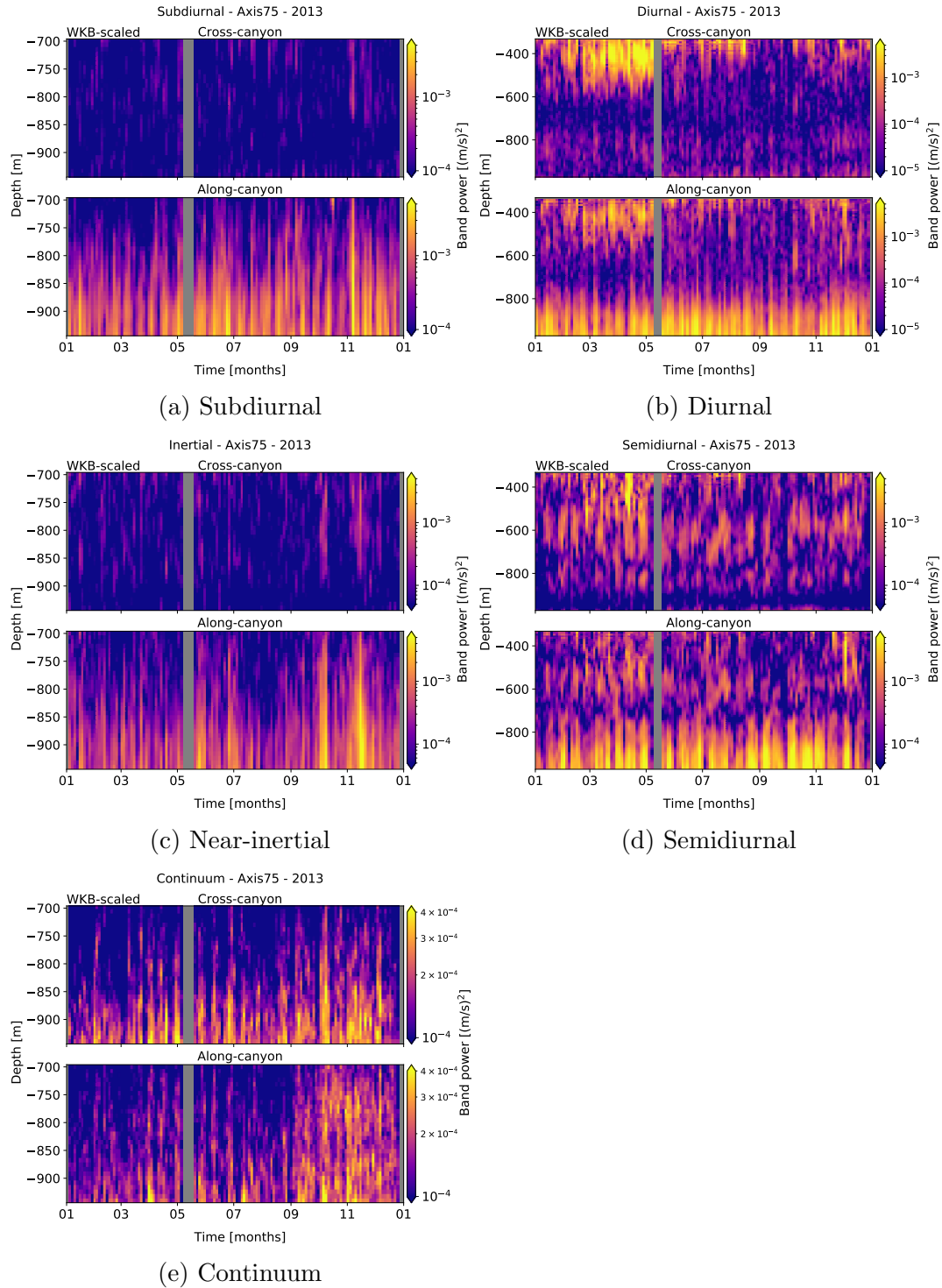


Figure 14: Band-integrated PSD data for Axis in 2013, for rotated, cleaned, and WKB-scaled horizontal velocity data. For each sub-figure, there are cross-slope (top) and along-slope (bottom) components. Intensity scales are adjusted for visual clarity of effects.

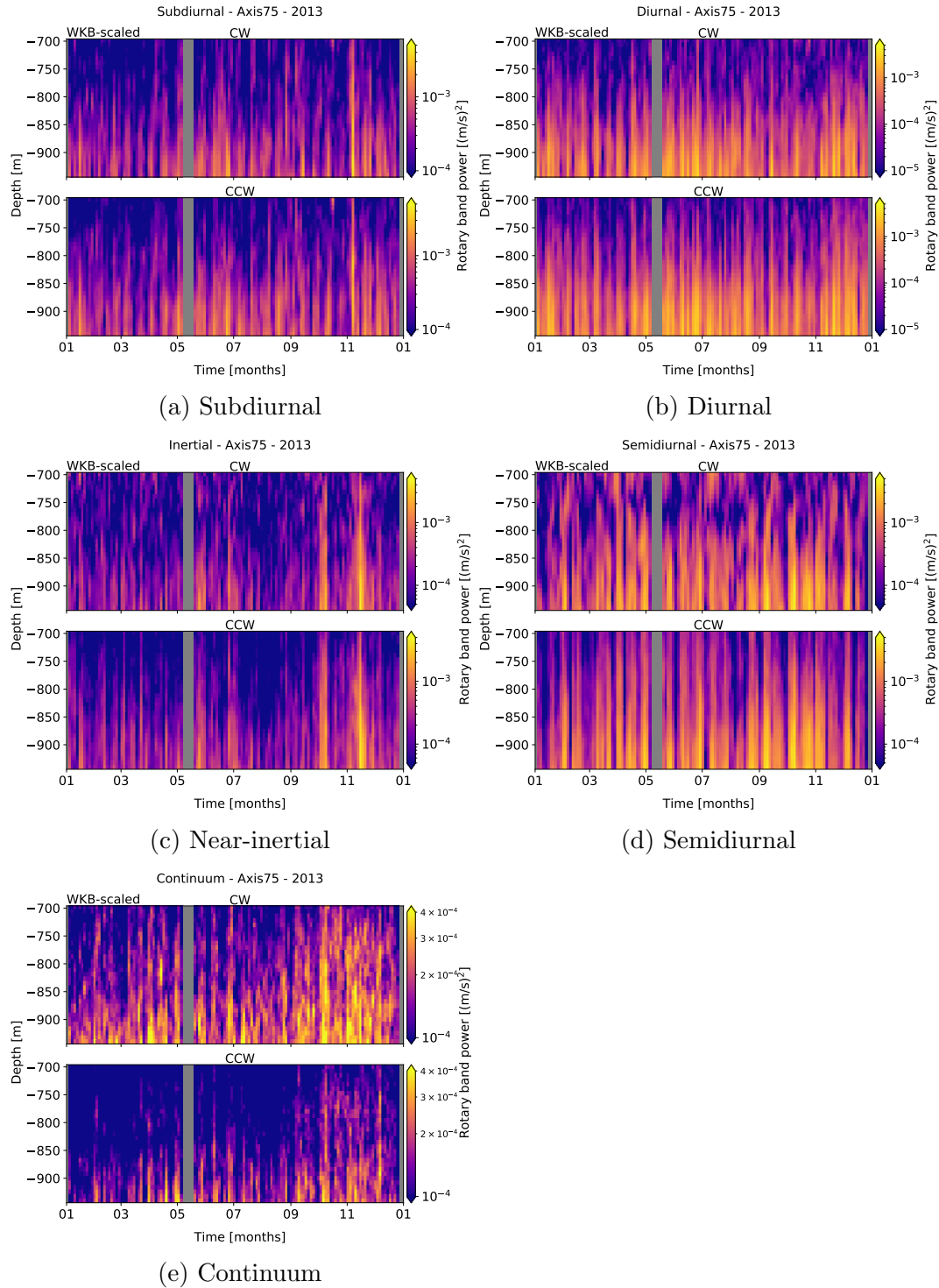


Figure 15: Band-integrated rotary data for Axis in 2013, for rotated, cleaned, and WKB-scaled horizontal velocity data. For each sub-figure, there are CW (top) and CCW (bottom) components. Intensity scales are adjusted for visual clarity of effects.

10 References

- Alford, M. H., MacKinnon, J. A., Zhao, Z., Pinkel, R., Klymak, J., & Peacock, T. (2007). Internal waves across the Pacific. *Geophysical Research Letters*, 34(24), 24601. <https://doi.org/10.1029/2007GL031566>
- Alford, M. H., Cronin, M. F., & Klymak, J. M. (2012). Annual cycle and depth penetration of wind-generated near-inertial internal waves at ocean station papa in the northeast pacific. *Journal of Physical Oceanography*, 42(6), 889–909. <https://doi.org/10.1175/JPO-D-11-092.1>
- Allen, S. E., Vindeirinho, C., Thomson, R. E., Foreman, M. G. G., & Mackas, D. L. (2001). Physical and biological processes over a submarine canyon during an upwelling event. *Canadian Journal of Fisheries and Aquatic Sciences*, 58(4), 671–684. <https://doi.org/10.1139/f01-008>
- Carter, G. S., & Gregg, M. C. (2002). Intense, variable mixing near the head of Monterey Submarine Canyon. In *Journal of Physical Oceanography* (Vol. 32). [https://doi.org/10.1175/1520-0485\(2002\)032;3145:IVMNTH;2.0.CO;2](https://doi.org/10.1175/1520-0485(2002)032;3145:IVMNTH;2.0.CO;2)
- Crawford, W. R., & Thomson, R. E. (1984). Diurnal-Period Continental Shelf Waves along Vancouver Island: A Comparison of Observations with Theoretical Models. *Journal of Physical Oceanography*, 14(10), 1629–1646. [https://doi.org/10.1175/1520-0485\(1984\)014;1629:dpcswa;2.0.co;2](https://doi.org/10.1175/1520-0485(1984)014;1629:dpcswa;2.0.co;2)
- Cummins, P. F., Masson, D., & Foreman, M. G. G. (2000). Stratification and mean flow effects on diurnal tidal currents off Vancouver Island. *Journal of Physical Oceanography*, 30(1), 15–30. [https://doi.org/10.1175/1520-0485\(2000\)030;0015:SAMFEO;2.0.CO;2](https://doi.org/10.1175/1520-0485(2000)030;0015:SAMFEO;2.0.CO;2)
- D’Asaro, E. A. (1985). The energy flux from the wind to near-inertial motions in the surface mixed layer. *J. Phys. Oceanogr.*, 15(8, Aug. 1985), 1043–1059. [https://doi.org/10.1175/1520-0485\(1985\)015;1043:tefftw;2.0.co;2](https://doi.org/10.1175/1520-0485(1985)015;1043:tefftw;2.0.co;2)
- Drakopoulos, P. G., & Marsden, R. F. (1993). The internal tide off the west coast of Vancouver Island. *Journal of Physical Oceanography*, 23(4), 758–775. [https://doi.org/10.1175/1520-0485\(1993\)023;0758:TITOTW;2.0.CO;2](https://doi.org/10.1175/1520-0485(1993)023;0758:TITOTW;2.0.CO;2)
- Garratt, J. R. (1977). Review of Drag Coefficients over Oceans and Continents. [https://doi.org/10.1175/1520-0493\(1977\)1052.0.CO;2](https://doi.org/10.1175/1520-0493(1977)1052.0.CO;2)
- Garrett, C., & Munk, W. (1979). Internal Waves in the Ocean. In *Ann. Rev.*

Fluid Mech (Vol. 11).

- Gemmrich, J., & Klymak, J. M. (2015). Dissipation of internal wave energy generated on a critical slope. *Journal of Physical Oceanography*, 45(9), 2221–2238. <https://doi.org/10.1175/JPO-D-14-0236.1>
- Gonella, J. (1972). A rotary-component method for analysing meteorological and oceanographic vector time series (Vol. 19). Pergamon Press.
- Hendershott, M. C., & Garrett, C. (2018). Internal Tides. In *Geophysical Fluid Dynamics* (No. 6). Retrieved from <https://gfd.whoi.edu/wp-content/uploads/sites/18/2018/03/lecture0621>
- Hotchkiss, F. S., & Wunsch, C. (1982). Internal waves in Hudson Canyon with possible geological implications. *Deep Sea Research Part A, Oceanographic Research Papers*, 29(4), 415–442. [https://doi.org/10.1016/0198-0149\(82\)90068-1](https://doi.org/10.1016/0198-0149(82)90068-1)
- Johnston, T. M. S., & Rudnick, D. L. (2015). Trapped diurnal internal tides, propagating semidiurnal internal tides, and mixing estimates in the California Current System from sustained glider observations, 2006-2012. *Deep-Sea Research Part II: Topical Studies in Oceanography*, 112, 61–78. <https://doi.org/10.1016/j.dsr2.2014.03.009>
- Klymak, J. M., Alford, M. H., Pinkel, R., Lien, R. C., Yang, Y. J., & Tang, T. Y. (2011). The breaking and scattering of the internal tide on a continental slope. *Journal of Physical Oceanography*, 41(5), 926–945. <https://doi.org/10.1175/2010JPO4500.1>
- Kundu, P. K., & Cohen, I. (2008). *Fluid mechanics*. (4th ed.). Academic Press.
- Kunze, E. (2017). Internal-wave-driven mixing: Global geography and budgets. *Journal of Physical Oceanography*, 47(6), 1325–1345. <https://doi.org/10.1175/JPO-D-16-0141.1>
- Kunze, E., Rosenfeld, L. K., Carter, G. S., & Gregg, M. C. (2002). Internal waves in Monterey Submarine Canyon. *Journal of Physical Oceanography*, 32(6), 1890–1913. [https://doi.org/10.1175/1520-0485\(2002\)032;1890:IWIMSC;2.0.CO;2](https://doi.org/10.1175/1520-0485(2002)032;1890:IWIMSC;2.0.CO;2)
- Kunze, E., Mackay, C., McPhee-Shaw, E. E., Morrice, K., Girton, J. B., & Terker, S. R. (2012). Turbulent mixing and exchange with interior waters on sloping boundaries. *Journal of Physical Oceanography*, 42(6), 910–927. <https://doi.org/10.1175/JPO-D-11-075.1>

- Kuroda, H., Kusaka, A., Isoda, Y., Honda, S., Ito, S., & Onitsuka, T. (2018). Diurnal tidal currents attributed to free baroclinic coastal-trapped waves on the Pacific shelf off the southeastern coast of Hokkaido, Japan. *Continental Shelf Research*, 158, 45–56. <https://doi.org/10.1016/j.csr.2018.02.010>
- Lamb, K. G. (2014). Internal wave breaking and dissipation mechanisms on the continental slope/shelf. *Annual Review of Fluid Mechanics*, 46, 231–254. <https://doi.org/10.1146/annurev-fluid-011212-140701>
- Levine, M. D. (2002). A modification of the Garrett-Munk internal wave spectrum. *Journal of Physical Oceanography*, 32(11), 3166–3181. [https://doi.org/10.1175/1520-0485\(2002\)032<3166:AMOTGM>2.0.CO;2](https://doi.org/10.1175/1520-0485(2002)032<3166:AMOTGM>2.0.CO;2)
- Li, M., Myers, P. G., & Freeland, H. (2005). An examination of historical mixed layer depths along Line P in the Gulf of Alaska. *Geophysical Research Letters*, 32(5), 1–4. <https://doi.org/10.1029/2004GL021911>
- Marques, O. B., Alford, M. H., Pinkel, R., MacKinnon, J. A., Klymak, J. M., Nash, J. D., ... Braznikov, D. (2020). Internal Tide Structure and Temporal Variability on the Reflective Continental Slope of South-eastern Tasmania. *Journal of Physical Oceanography*, 51(2), 611–631. <https://doi.org/10.1175/jpo-d-20-0044.1>
- Martini, K. I., Alford, M. H., Kunze, E., Kelly, S. M., & Nash, J. D. (2013). Internal bores and breaking internal tides on the Oregon continental slope. *Journal of Physical Oceanography*, 43(1), 120–139. <https://doi.org/10.1175/JPO-D-12-030.1>
- Mihaly, S. F., Thomson, R. E., & Rabinovich, A. B. (1998). Evidence for non-linear interaction between internal waves of inertial and semidiurnal frequency. *Geophysical Research Letters*, 25(8), 1205–1208. <https://doi.org/10.1029/98GL00722>
- Munk, W., & Garrett, C. (1979). Internal Waves and Small-Scale Processes. In C. Wunsch (Ed.), *Evolution of Physical Oceanography*.
- Nash, J. D., Kunze, E., Toole, J. M., & Schmitt, R. W. (2004). Internal tide reflection and turbulent mixing on the continental slope. In *Journal of Physical Oceanography* (Vol. 34). [https://doi.org/10.1175/1520-0485\(2004\)034<1117:ITRATM>2.0.CO;2](https://doi.org/10.1175/1520-0485(2004)034<1117:ITRATM>2.0.CO;2)
- Polzin, K. L., & Lvov, Y. V. (2011). Toward regional characterizations of the oceanic internal wavefield. *Reviews of Geophysics*, 49(4), 4003. <https://doi.org/10.1029/2010RG000329>

- Robertson, R., Dong, J., & Hartlipp, P. (2017). Diurnal Critical Latitude and the Latitude Dependence of Internal Tides, Internal Waves, and Mixing Based on Barcoo Seamount. *Journal of Geophysical Research: Oceans*, 122(10), 7838–7866. <https://doi.org/10.1002/2016JC012591>
- Subeesh, M. P., Unnikrishnan, A. S., & Francis, P. A. (2021). Generation, propagation and dissipation of internal tides on the continental shelf and slope off the west coast of India. *Continental Shelf Research*, 214. <https://doi.org/10.1016/j.csr.2020.104321>
- Terker, S. R., Garton, J. B., Kunze, E., Klymak, J. M., & Pinkel, R. (2014). Observations of the internal tide on the California continental margin near Monterey Bay. *Continental Shelf Research*, 82, 60–71. <https://doi.org/10.1016/j.csr.2014.01.017>
- Thomson, R. E., & Crawford, W. R. (1982). The Generation of Diurnal Period Shelf Waves by Tidal Currents in: *Journal of Physical Oceanography* Volume 12 Issue 7 (1982). *Journal of Physical Oceanography*, 12(7).
- Thomson, R. E., Roth, S. E., & Dymond, J. (1990). Near-inertial motions over a mid-ocean ridge: Effects of topography and hydrothermal plumes. *Journal of Geophysical Research*, 95(C5), 7261. <https://doi.org/10.1029/jc095ic05p07261>
- Thomson, R. E., & Fine, I. V. (2003). Estimating mixed layer depth from oceanic profile data. *Journal of Atmospheric and Oceanic Technology*, 20(2), 319–329. [https://doi.org/10.1175/1520-0426\(2003\)020<0319:EMLDFO>2.0.CO;2](https://doi.org/10.1175/1520-0426(2003)020<0319:EMLDFO>2.0.CO;2)
- Thomson, R. E., & Emery, W. J. (2014). *Data Analysis Methods in Physical Oceanography: Third Edition*. In *Data Analysis Methods in Physical Oceanography: Third Edition* (Third). <https://doi.org/10.1016/C2010-0-66362-0>
- Thomson, R. E., & Krassovski, M. V. (2015). Remote alongshore winds drive variability of the California Undercurrent off the British Columbia-Washington coast. *Journal of Geophysical Research: Oceans*, 120(12), 8151–8176. <https://doi.org/10.1002/2015JC011306>
- Voelker, G. S., Olbers, D., Walter, M., Mertens, C., & Myers, P. G. (2020). Estimates of wind power and radiative near-inertial internal wave flux: The hybrid slab model and its application to the North Atlantic. *Ocean Dynamics*, 70(11), 1357–1376. <https://doi.org/10.1007/s10236-020-01388-y>
- Xie, X., & Chen, D. (2021). Near-surface reflection and nonlinear effects

- of low-mode internal tides on a continental slope. *Journal of Physical Oceanography*, 51(4), 1037–1051. <https://doi.org/10.1175/JPO-D-20-0197.1>
- Xie, X., Liu, Q., Zhao, Z., Shang, X., Cai, S., Wang, D., & Chen, D. (2018). Deep Sea Currents Driven by Breaking Internal Tides on the Continental Slope. *Geophysical Research Letters*, 45(12), 6160–6166. <https://doi.org/10.1029/2018GL078372>
- Zheng, J., Tian, J., & Liang, H. (2017). Observation of near-inertial internal waves on the continental slope in the northwestern South China Sea. *Journal of Ocean University of China*, 16(2), 184–190. <https://doi.org/10.1007/s11802-017-3153-7>